Structures 47 (2023) 482–499

Contents lists available at ScienceDirect

Structures

journal homepage: www.elsevier.com/locate/structures

A rapid machine learning-based damage detection algorithm for identifying the extent of damage in concrete shear-wall buildings

Hossein Mahmoudi [a], Maryam Bitaraf [a], Mojtaba Salkhordeh [b], Siavash Soroushian [b,*]

[a] Department of Civil and Environmental Engineering, University of Tehran, Tehran, Iran
[b] Department of Civil and Environmental Engineering, K. N. Toosi University of Technology, Tehran, Iran

ARTICLE INFO

Keywords:
Concrete shear wall
Machine learning
Damage detection
Ground motion
Cumulative absolute velocity

ABSTRACT

This paper presents a rapid machine learning-based damage detection framework for identifying the damage extent of concrete shear wall buildings. For this purpose, a parametric study was carried out to determine the most efficient machine learning algorithm in classifying the damage states of the building. According to this parametric study, the K-Nearest Neighbor (KNN) learner was selected as the reference prediction model because of the higher accuracy achieved by this algorithm. Bayesian Optimization (BO) algorithm was used to tune the hyperparameters affecting the accuracy of the model. The most efficient attributes were selected from the set of damage indicators through the BO algorithm to train the model. Three different benchmark buildings, including 7-,9-, and 13-story concrete shear wall buildings, were used to evaluate the robustness of the proposed framework. A suite of 111 pair motions, originally developed for the SAC project, were employed to create a generalized dataset. These motions were uniformly scaled from 0.05 g to 1.5 g to expand the intensity range of the events. All the acceleration signals were polluted to 10% noise using white Gaussian signals to simulate the field condition. Results reveal the efficiency of the proposed framework in identifying the extent of damage in concrete shear wall elements of the building. In addition, a parametric study was conducted to illustrate the reliability of two commonly used features, called Cumulative Absolute Velocity (CAV) and the energy ratio between the acceleration response and the input excitation, in determining the damage states of the shear walls under seismic motions.

1. Introduction

Assessment of structural safety is essential for post-earthquake restoration. Generally, to evaluate the post-earthquake vitality of the exposed structures, a complete visual inspection is required [1]. Coordination and implementation of the manual visual inspection needs several dedicated teams and monetary resources. In this regard, considerable efforts have been carried out to automate the visual inspection process, e.g., image-based visual inspection [2]. However, such an engineering visual inspection is only able to detect the visible defects that occurred in the structures [3]. This means that some serious invisible damages may be left latent during the visual inspection. The process of identifying and tracking the structural damage is known as the Structural Health Monitoring (SHM) [4,5]. In SHM, damage detection is related to the methods developed for identifying the probable existence, severity, and location of the structural damage. Model-based and data-driven methods are two of the most commonly used strategies proposed for damage detection. Model-based methods generally involve a system identification algorithm paired with a finite element analysis to update the structural model [6]. The performance of the model-based approaches directly depends on the accuracy of the information about the physical properties of the under-study structure. In addition, updating the finite element model based on the physical properties of the structure is computationally expensive for large-scale structures, and rapid condition monitoring could be challenging in this condition [7,8]. On the other hand, data-driven methods apply statistical learning algorithms to the vibration data captured from the structure. This method uses learning algorithms to construct a classification or regression learner for predicting structural damage [9,10]. Tsou and Shen [11] proposed the use of Neural Networks (NNs) for predicting the severity and location of the structural damage. They used the variations in the modal properties of the structure as the damage feature to identify the damage. Worden et al. [12] proposed outlier analysis to compute the deviation of structural response from its normal condition for detecting the damage by solving a novelty detection problem. Zhao et al. [13] explored the efficiency of counter-propagation NNs to locate the structural damage and identify the

* Corresponding author.
E-mail address: ssoroushian@kntu.ac.ir (S. Soroushian).

https://doi.org/10.1016/j.istruc.2022.11.041
Received 5 October 2022; Received in revised form 9 November 2022; Accepted 11 November 2022
Available online 28 November 2022

(a) Crushing and rebar local buckling at the end of the wall (b) Concrete crushing accompained by buckling of the vertical rebars

Fig. 1. Failure mechanisms of the concrete shear walls during the 2010 Chile earthquake.

support movement of beams in their axial direction. Yam et al. [14] presented a method based on capturing the variations in the energy of the structural vibrations using wavelet transform and Artificial Neural Networks (ANNs). Zhang et al. [15] proposed the regression tree and random forest to evaluate the post-earthquake structural safety. Sajedi and Liang [16] proposed a near real-time damage detection framework based on a fully convolutional encoder–decoder NN. Salkhordeh et al. [17] proposed a decision-tree based algorithm for identifying the structural damage in braced-frame buildings. Neves et al. [18] presented a dynamic decision-making algorithm to conduct the structural health monitoring in bridges. They used the Bayesian theorem to update the prior possibilities of the structural condition based on the new information provided by the system. Different optimization algorithms can be used to tune the hyperparameters of the machine learning algorithms [19–22]. In general, the application of signal processing methods along with machine learning algorithms plays an imperative role in implementing these approaches [1,1,23,24].

Feature extraction and compressing the size of damage index vector are two important objectives of implementing a classification algorithm. The main object of reducing the size of the dataset is to ameliorate the learning performance and rate of the learning problem. Principal Component analysis (PCA) [25], Locally Linear Embedding (LLE) [26], and Independent Component analysis (ICA) [27] are well-known tools in data size compression. Several studies were carried out to find low-dimensional features that could be used as the damage index in the SHM. This low-dimensional features aim to avoid fitting sophisticated statistical models to the response time series. Reed and Kassawara [28] proposed two damage indicators based on Cumulative Absolute Velocity (CAV) and response spectrum acceleration to determine the existence of damage in the structures. Cabanas et al. [29] proposed the modified CAV and Arias intensity (I_A) as two damage indexes that have an appropriate correlation with the damage. Bandara et al. [30] presented a damage index based on the Principal Components (PCs) of the Frequency Response Functions (FRF) of the structure. Muin and Mosalam [31] investigated the performance of CAV for localizing the structural damage in structural systems. Sajedi and Liang [32] presented two features based on the energy ratio of the structural response for detecting the damage. Salkhordeh et al. [17] showed that the features based on the energy ratio of the structural response are not efficient as a dependent attribute to classify the structural damage after the earthquake. They combined an energy-based feature with two additional attributes, including drift ratio extracted from acceleration response and the correlation coefficient between the linear and nonlinear response of the structure. These damage indicators were employed to identify the extent of damage based on the recommendations of ASCE-41 [33] for braced-frame buildings. Selecting efficient features depends on the structural properties and the type of application that is expected from the method [34,35].

Previous earthquakes show that the damage intensity is significantly varied in buildings [36]. The extent of damage could be either visible due to the large deformations in different elements or hidden because of the slight deflection in that elements. For example, primitive evaluation of a building subjected to the 1994 Northridge earthquake demonstrated that the structural elements had not suffered extensive damage. However, by eliminating the nonstructural components, the site engineers reported that the dynamic performance of the building is highly reduced due to the failure of structural elements [37]. Reinforced concrete shear walls are widely used to provide the lateral load resistance of buildings under earthquake motions because of their high stiffness and strength. Experimental investigations illustrated that the seismic performance of shear walls is different regarding the wall characteristics. In general, short wall response is dominated by shear and slender wall response governed by flexural behavior [38,39]. Fig. 1 shows failure mechanisms of concrete shear walls during the 2010 Chile earthquake.

As shown in this figure, extensive crushing of the concrete followed by local buckling of the rebars led to the complete collapse of the walls. More than 100 concrete shear wall buildings were severely damaged during the 2010 Chile earthquake (Mw = 8.8) [40]. In the light of these experiences, it can be concluded that implementing a monitoring scheme in these buildings is essential not only for mitigating the lifetime damages but also for early identifying the post-earthquake damages. According to the previous studies, there are two main research gaps in (1) rapid estimation of the local damage exposed to the shear-walls of concrete buildings and (2) investigating the efficiency of different damage features derived from the ground motion records and the structural response in identifying the local damage of the structure caused by ground motions. In addition, in machine-learning-based structural health monitoring, a finite number of studies investigated the most powerful learning algorithm as well as damage indices for detecting the structural damage.

This paper presents a machine-learning-based damage detection framework for identifying the extent of damage exposed to the concrete shear-wall buildings during the earthquake. For this purpose, a series of nonlinear response history analyses are implemented on three 3D (three-dimensional) buildings using a suite of 111 ground motions that

Table 1
Material properties of steel rebars.

Element	Yield strength (ksi)	Modulus of elasticity (ksi)	Strain hardening ratio
Steel rebar grade $AIII$	58	29000	0.01

Table 2
Material properties of concrete.

Confinement type	Expected compressive strength (ksi)	Strain at maximum strength	Crushing strength	Strain at crushing strength
Confined concrete	5.55	0.003	1.11	0.03
Unconfined concrete	4.26	0.003	0.85	0.01

Table 3
Results of mesh sensitivity analysis.

Model	Mesh size	IDR_{max}	Analysis time	Error
1	0.5 m × 0.5 m	0.0173	$5^{h}, 10^{min}$	–
2	1.0 m × 1.0 m	0.0177	$1^{h}, 17^{min}$	2.3%
3	1.5 m × 1.5 m	0.0213	58^{min}	23.1%
4	2.0 m × 2.0 m	0.0228	34^{min}	31.8%

originally developed in the SAC project [41]. To increase the rate of training and eliminate unnecessary features, Bayesian Optimization (BO) is applied. In addition, hyperparameters of the classification learner are optimized by using the BO algorithm. This paper sheds significant light on rapid damage estimation of concrete shear-wall buildings using machine-learning techniques. The present paper is organized in such a way that first, the benchmark buildings and their modeling procedure are described. Then, the damage indicators derived from the vibration data recorded during the earthquake motions are introduced. Next, different classification algorithms (i.e. decision trees, support vector machine, k-nearest neighbor, linear discriminant analysis, and Naive Bayes) used to achieve the best classification learner are explained. In subsequent, the implementation procedure of the proposed framework is presented. Finally, the results obtained for determining the extent of damage in benchmark structures (concrete shear wall buildings) are discussed.

2. Benchmark buildings

This study aims to predict the structural damage in concrete shear-wall buildings after a damaging earthquake. To investigate the efficiency of the proposed method, three existing 7-, 9-, and 13-story concrete shear wall buildings were used as the benchmark models. These buildings were designed in high seismic zone according to the corresponding modern code. The modeling procedure and the structural details of these benchmark buildings are explained in the next subsections.

2.1. Seven-story building

A 3D seven-story building is selected to assess the performance of the proposed method in identifying the structural damage of concrete shear wall buildings. This building includes two shear walls continued through all the stories. Fig. 2 shows a general view of the building as well as its plan view. It is worthwhile to mention that the first three natural periods of the structure were respectively equal to 1.27 s, 0.66 s, and 0.45 s.

2.2. Nine-story building

The second case study model was an existing nine-story concrete shear wall building. As shown in Fig. 3, this building had a core as well as a single shear wall that continued from the underground level to the roof level. The remaining walls shown in Fig. 3(b) only belonged to the underground floors. It is notable that the first three fundamental periods of the structure were respectively 1.63 s, 0.83 s, and 0.54 s.

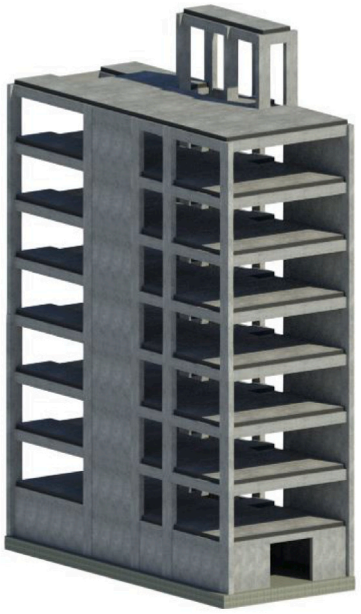

(a) 3D view

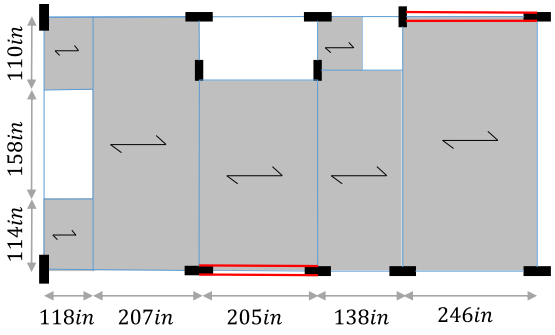

(b) Plan view

Fig. 2. General view of the 7-story building.

2.3. Thirteen-story building

The third case study model was an existing thirteen-story concrete shear wall building. Fig. 4 shows a general view of this model as well as its plan view. According to this figure, this building has six concrete shear walls continued through all the stories of the structure. The first three natural periods of the building were equal to 1.99 s, 1.84 s, and 0.76 s. The modeling details of the benchmark buildings are explained in the following section.

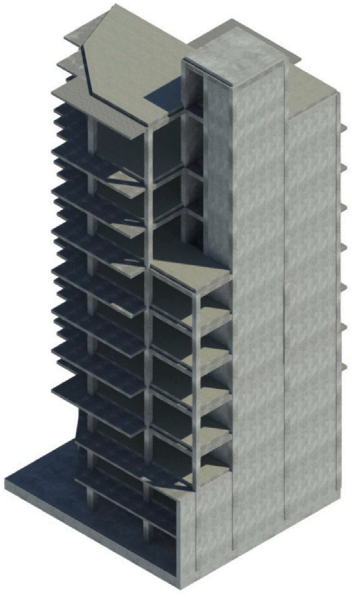

(a) 3D view

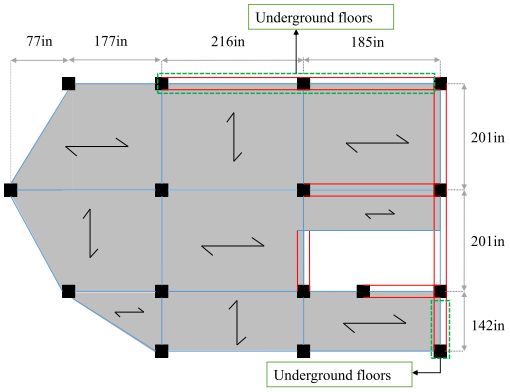

(b) Plan view

Fig. 3. General view of the 9-story building.

(a) 3D view

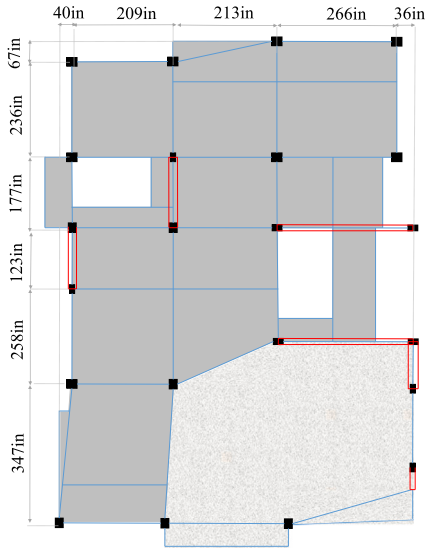

(b) Plan view

Fig. 4. General view of the 13-story building.

2.4. Numerical modeling methodology

All the steel rebars are modeled using the Giuffre-Menegotto-Menegotto-Pinto uniaxial strain-hardening material model defined as *Steel*02 is *Opensees* platform. The yield stress and modulus of elasticity for *AIII* steel bars were 58.0 ksi and 29000 ksi, respectively. In addition, the strain hardening ratio of steel material was designated as 0.01. The recommended values of 0.15, 0.925, and 12 were respectively considered for the model parameters $cR2$, $cR1$ and $R0$ to control the shape of hysteresis curves of the rebars. These parameters control the transition of the hysteresis curve from elastic region to plastic branch. The isotropic hardening parameters $a1$, $a2$, $a3$, and $a4$ defined as the default values of 1.0, 0, 1.0 and 0, respectively. Table 1 summarizes the material properties of the steel rebars considered for reinforced concrete elements. Cross-sectional properties of concrete beams and columns were defined using the *FiberSection* command in *Opensees*. The material model of both confined and unconfined concrete was defined using the model presented by Yassin [42] which is designated in *OpenSees* as *Concrete*02. For unconfined concrete, the expected compressive strength f_{pc} was 4.26 ksi, the concrete strain e_{psc0} at maximum strength was 0.003 (which represents an initial concrete modulus (E_0) equal to that defined in ACI 318 [43]), the concrete crushing strength $f_{pcu} = 0.2f_{pc}$ and the concrete strain at crushing strength was $e_{psU} = 0.01$. The parameters f_pc and e_{psc0} for confined concrete were calculated using the recommendation of Saatcioglu and Razvi [44], depending on the area, spacing, and configuration of the transverse reinforcement. For the confined concrete, the expected compressive strength fpc was 5.55 ksi. Similar to the unconfined concrete, the crushing strength of confined concrete was also considered equal to $0.2f_{pc}$. The crushing strain of the confined concrete was considered similar to the compression strain ϵ_{20} of the Saatcioglu and Razvi model [44]. The ratio between the unloading slope and the initial slope was selected to be the default value of 0.1. The tensile strength of concrete f_t was considered as $0.33\sqrt{f'_c}$ [45] and the softening stiffness of concrete in tension E_{ts} was defined as $0.05E_0$ according to the recommendation of Yassin [42].

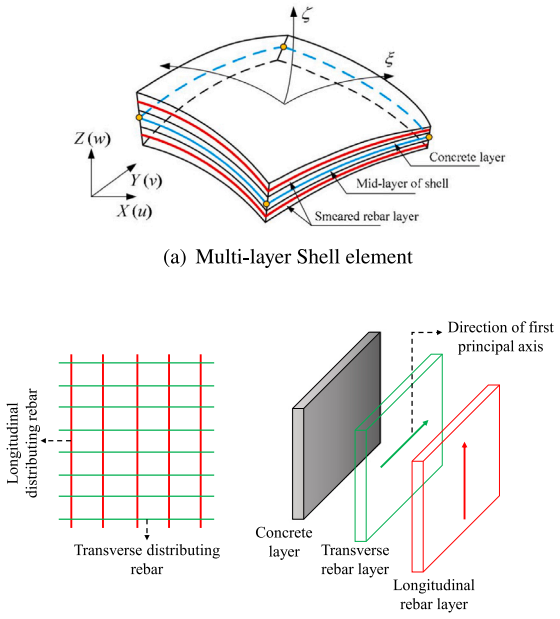

(a) Multi-layer Shell element

(b) Distribution of different layers of the wall

Fig. 5. Shell element for modeling the concrete shear walls [46].

Table 2 shows the material properties of both confined and unconfined concrete used for all the case studies. All the beam and column elements were modeled using the displacement-based beam–column element. The shear wall elements were assigned to the structure using the *ShellNLDKGQ* element. Material properties of each layer and corresponding geometrical characteristics of the wall can be assigned to this element as shown in Fig. 5(a). This element is developed to take into account the geometric nonlinearity of large deformations using the updated Lagrangian method. The *ShellNLDKGQ* element simplifies the nonlinear behavior of 3D concrete shear walls by discretizing different elements of the wall into separate fully-bonded layers along the thickness direction. *LayeredShell* command was used to create the fiber-based multi-layer section of the shear walls. As shown in Fig. 5(b), the rebars are defined as spread orthotropic layers considering the direction and location of them. The axial strain and curvature of the middle layer is firstly calculated. Then, the strain of other layers is calculated by applying the plane-section assumption [46,47].

Remarkably, all the slabs were defined as rigid diaphragms in both horizontal directions. Since the size of meshes considered for the shear wall elements highly affects the computational time, a mesh sensitivity analysis was performed to achieve an optimum model with acceptable accuracy and analysis time. Fig. 6 shows the effect of meshing size on the inter-story drift ratio of the building. In addition, Table 3 shows the results of mesh sensitivity analysis for 7-story building. This Table summarizes the computational time and maximum inter-story drift ratio of the building under the *CoyoteLake* earthquake record. As can be seen, the size of mesh was selected as 1.0 m×1.0 m because of promising accuracy and computational time compared to the 0.5 m×0.5 m meshing size.

3. Feature extraction

Vibration-based damage detection methods highly depends on the damage index used for revealing the extent of the damage. This paper uses seven different damage features and investigates the efficiency of these attributes in diagnosing the extent of damage in concrete shear wall buildings. This research reduced the number of damage features by selecting efficient attributes from the set of features through

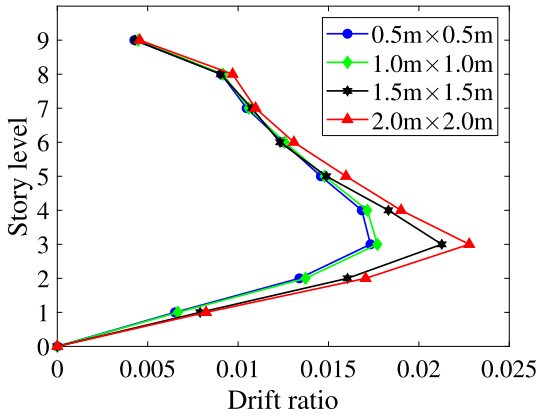

Fig. 6. Inter-story drift ratio of the structure for different mesh sizes.

Bayesian optimization [48]. Doing so leads to increasing the learning rate of the classifier and reducing the computational cost. The following subsections are going to explain these damage indexes.

3.1. Arias intensity (I_A)

Cabanas et al. [29] proved that the Arias intensity of the ground motions is related to the severity of damage in earthquake-exposed buildings. The Arias intensity of a signal can be defined as follow:

$$A_I = \frac{\pi}{2g}\int_0^t (\ddot{u}(t))^2 dt \tag{1}$$

where $\ddot{u}(t)$ is the earthquake acceleration at time step t. Since the Arias intensity measure does not include any information about the structural properties, this index is not accurate in identifying the local damage in structural elements. For example, different ground motions may have similar input energies, but impose different damage severities to the building because of differences in the frequency content of the records.

3.2. Cumulative Absolute Velocity (CAV)

As mentioned before, Reed and Kassawara [28] illustrated that the CAV is correlated with the extent of damage that imposed to the structure during an earthquake. The CAV of the structural response can be written as below:

$$CAV = \int_0^T |a(t)|\, dt \tag{2}$$

where T is the duration of the structural response, a is the acceleration response of the building's floor. Unlike the Arias intensity, the CAV criterion includes the nonlinearity condition of the structure. However, the value of CAV highly depends on the duration of the ground motion record. For instance, a ground motion with a lower value of PGA and a larger duration may results in a larger value of CAV compared to a record with a larger PGA and lower duration.

3.3. Modified Cumulative Absolute Velocity (MCAV)

According to the study implemented by Salkhordeh et al. [17], the CAV may not be efficient in detecting the extent of damage because of its dependence on the earthquake duration. Therefore, this study uses the Modified Cumulative Absolute Velocity (MCAV) as one of the damage features. The MCAV attribute is written as below:

$$MCAV = \sum_{i=1}^{N}(H(PGA_i - c)\int_{i-1}^{i} |a(t)|dt) \tag{3}$$

where N is the number of one-second time intervals of the ground motion, $H(x)$ is the Heaviside step function defined as 0 for $x \prec 0$ and

1 for $x > 0$, PGA_i is the peak ground acceleration for ith time interval, and c is a PGA threshold to neglect the summation for values smaller than this threshold value [49].

3.4. Spectral acceleration

It seems necessary to define a damage indicator that includes both characteristics of the structure and input ground motions. To do so, the spectral acceleration of the earthquake records at the first fundamental period of the building is defined as a damage feature. This attribute enables the framework to learn the extent of damage based on the intensity of ground motion and also the dynamic properties of the building.

3.5. Energy ratio

Damage severity in a building has a direct relation to the nonlinearity that occurred in the structural elements [9]. This nonlinearity is estimable from the acceleration response of the structure. To capture the nonlinearity in the structure, a relative energy ratio is defined below:

$$RE = \frac{\int_0^T |\ddot{u}(t)|\, dt}{\int_0^T \left|\ddot{u}_g(t)\right| dt} \tag{4}$$

where, $\ddot{u}(t)$ and $\ddot{u}_g(t)$ are the recorded acceleration from the floor and ground level of the structure, respectively. Nonlinearity in the structural elements leads to the change in the relative ratio of CAV in different Degree of Freedoms (DOFs) of the building.

3.6. Drift

It is well-understood that the severity of damage exposed to the building under the earthquake motions has a direct relation with the inter-story drift [50]. Ideally, the story drift time–history can be computed by implementing two consecutive integration on the relative acceleration response of the structure. However, there is an unwanted noise in the acceleration response histories captured by the accelerometers. This makes the obtained drift history unreliable. Therefore, signals acquired by sensors should be filtered from noise by using the process known as "de-noising". The present study implements the non-parametric de-noising approach known as "wavelet shrinkage denoising". This method was originally developed by Donoho et al. [51–54]. The wavelet function $\psi(t) \in L^2(\Re)$ can be written as follow [55]:

$$\psi_{a,b}(t) = |a|^{-0.5}\, \psi\left(\frac{t-b}{a}\right) \tag{5}$$

where $L^2(\Re)$ represent the suite of integrable functions, a and b are respectively the scale and translation factors, $|a|^{-0.5}$ is defined to normalize the value of $\|\psi_{a,b}\|$, and ψ is the wavelet function. The wavelet function has a zero mean value, and must meet the admissibility condition as below:

$$C_\psi = \int_{-\infty}^{\infty} \frac{|\hat{\psi}(\omega)|^2}{|\omega|} d\omega < \infty \tag{6}$$

where ω refer to the frequency, and $\hat{\psi}(\omega) = \int_{\Re} \psi(x) \exp(-ix\omega) dx$ is the Fourier transform of the function ψ. The inner product of the wavelet families $\psi_{a,b}(t)$ to the signal $x(t)$ is defined as Continuous Wavelet Transform (CWT):

$$F_W(a,b) = \prec x(t), \psi_{a,b}(t) \succ = \int_{-\infty}^{\infty} x(t) \frac{1}{\sqrt{a}} \psi^*\left(\frac{t-b}{a}\right) dt \tag{7}$$

where ψ^* indicates the complex conjugate of ψ. This equation converts to the Discrete Wavelet Transform (DWT) where parameters a and b are defined as discrete values. To reconstruct the signal $x(t)$ from its wavelet transform, Calderon's identity can be written as below:

$$x(t) = \frac{1}{C_\psi} \int_{-\infty}^{\infty} \int_{-\infty}^{\infty} F_W(a,b) \psi\left(\frac{t-b}{a}\right) \frac{da}{a^2} \frac{db}{\sqrt{b}} \tag{8}$$

Notably, this method is different with the conventional linear filtering approaches because of implementing a nonlinear shrinkage on coefficients in the transform domain. Moreover, the conventional de-noising methods assume the low signal-to-noise ratio for the signal, which may apply additional bias to the filtered signal. In addition, unlike the parametric methods that need an initial approximation of the model parameters, wavelet de-noising approaches are non-parametric, and the correction is related to specific properties of the signal. Hence, wavelet de-noising approach is applied in this study to prepare the noisy signal for integration. Fundamental characteristics required to implement the method were defined same as the recommendations of Ansari et al. [56],Soroushian et al. [57], which evaluate the efficiency of wavelet multi-resolution analysis in correcting the noisy signals. This method includes two phases based on wavelet de-noising to modify the acceleration time histories.

In the first phase, the signal decomposes into N levels, in which the N value is selected to achieve the frequency range of interest for the Nth detail of the signal. Next, two modifiers are subjected to the detail values of the signal if its amplitude violate a pre-defined threshold level [51–54] The modification functions depend on the single positive parameter η, called the threshold as:

$$Soft\ thresholding: T_s(D,\eta) = \begin{cases} D-\eta, & D \geq \eta \\ 0, & |D| \prec \eta \\ D+\eta, & D \leq -\eta \end{cases} \tag{9}$$

$$Hard\ thresholding: T_s(D,\eta) = \begin{cases} 0, & |D| \prec \eta \\ D, & |D| \geq \eta \end{cases} \tag{10}$$

Generally, thresholds can be classified into two categories: (1) "single thresholds" and (2) "level-dependent thresholds". In the first method, a single threshold determined according to the properties of the signal is imposed to the wavelet coefficients. In the second approach, the threshold values are determined regarding the characteristics of the signal at different levels. After the thresholding step, the corrected signal was reconstructed according to its approximation and detail values.

The second phase has the same steps as the first one, and only the following differences should be considered.

- Modification factors are used for the velocity signal obtained by applying multiple integration to the acceleration response achieved in the first phase.
- The velocity signal should be parsed to M levels (where $M \geq (N+2)$).
- After the thresholding step, the modified velocity signal is reconstructed by applying a summation on only the details of the velocity signal.

It should be mentioned that the first phase is useful for modifying the high-frequency noises, and the second phase is suitable for correcting the low-frequency noises of the signal. In this study, according to the study of Soroushian et al. [57], hard-thresholding is used together with the SureShrink approach to modify the acceleration signals. Notably, SureShrink is an efficient approach for computing the level-dependent thresholds. In addition, to prevent the phase distortion that is usual in conventional methods of de-noising, the symlet wavelet is used because of its approximately linear phase response [56]. For example, Fig. 7 shows the result of using "wavelet de-noising" for correcting the drift response of the first floor of 9-building under the $CoyoteLake$ earthquake (26.86s duration) in presence of 10% noise. This Figure also illustrates a drift response that is directly calculated from the acceleration response of the building polluted with 5% noise. It is clear that the drift response obtained through direct integrating on the acceleration history is far from the real response even when the acceleration response of the building contains 5% noise. However, the corrected drift history is well-correlated with the response of the building. It should be noted that the "wavelet de-noising" approach may not be efficient for certain response because of different frequency content of the ground motions.

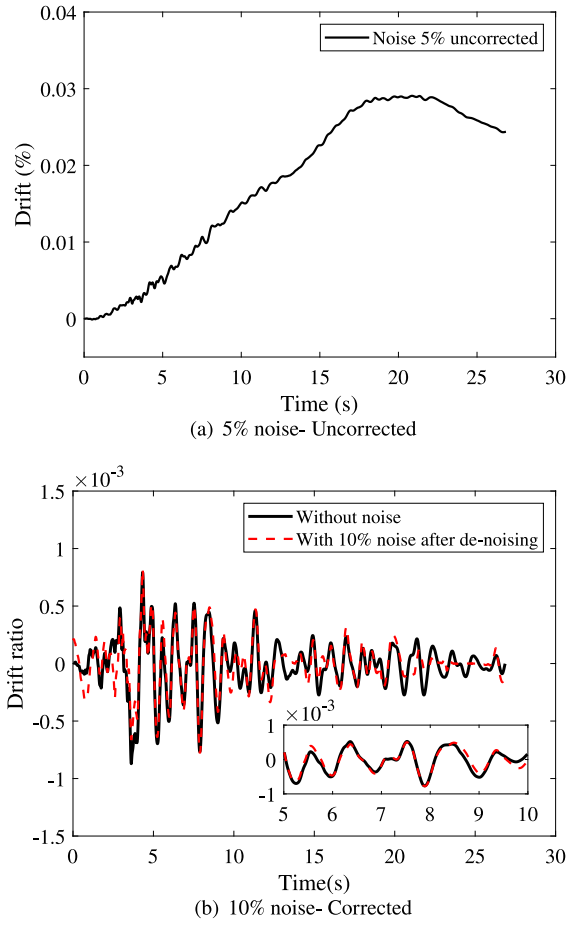

Fig. 7. Efficiency of the "wavelet de-noising" in correcting the drift response.

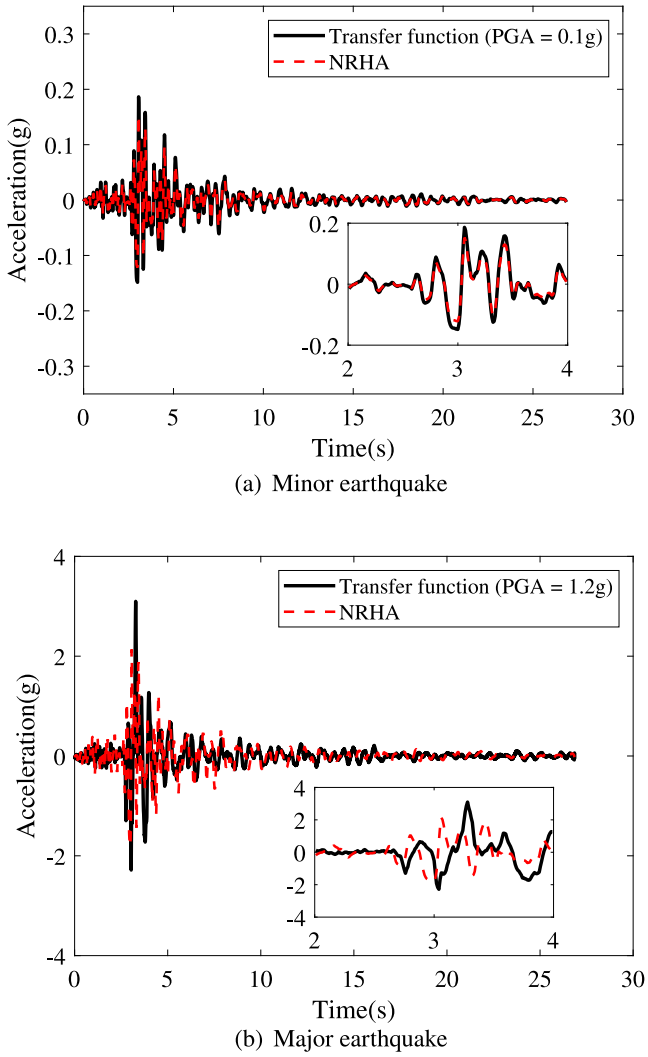

Fig. 8. The effect of nonlinearity on the correlation coefficient damage indicator.

3.7. Correlation coefficient

THe correlation coefficient between the nonlinear acceleration response of the building (real structure) and the acceleration response obtained from the corresponding linear system was used as a damage indicator. A linear and time-invariant transfer function $H(\omega)$ was defined as the proportion of the response signal y and input excitation x as below:

$$H(\omega) = \frac{S_{yy}(\omega)}{S_{xy}(\omega)} \tag{11}$$

where S_{xy} represent the cross power spectral density between the excitation and response signals, and S_{yy} is the power spectral density of the acceleration response of the structure. The equivalent linear response of the building, $y(t)$, is estimable by calculating the inverse Fourier transform of $H(\omega)X(\omega)$, where $X(\omega)$ is the Fourier spectrum of the input excitation. The transfer function of a structure can be obtained by: (1) using sensory data acquired from the minor ground motions recorded during the lifetime of the structure, or (2) by conducting an ambient vibration-based experiment [58]. In the present research, the acceleration response of the building under a minor earthquake is used to calculate the transfer function of the structure.

In general, by increasing the severity of damage in the building, the acceleration response deviates more from the response of the equivalent linear system because of nonlinearity in the structural elements. Fig. 8 illustrates this matter for two examples, one for the response of the structure under the scaled $CoyoteLake$ ground motion with PGA = 0.1 g and another for PGA = 1.2 g. It is obvious that whatever the ground motion intensity increases, the correlation coefficient between these responses becomes lower (close to zero for severe damage). The correlation of two signals depends on the intensity of the relationship between the relative movements of these two signals [59]. Here, the correlation coefficient between the nonlinear response of the building (real building) and corresponding linear system was written as follow:

$$C_{X,Y} = \rho_{x,y} = \frac{E[(X - m_X)(Y - m_Y)]}{\sigma_X \sigma_Y} \tag{12}$$

where, X was the acceleration response recorded from the structure, and Y was the acceleration response of the equivalent linear system. Moreover, m_X and m_Y were the average values of the acceleration response for the real building and its equivalent linear system, respectively.

4. Machine learning algorithms

Machine learning algorithms are extensively progressed in earthquake engineering, especially for damage detection, system identification, and risk assessment applications. This paper implements a parametric study to determine the best classification learner among the Support Vector Machine (SVM), K-Nearest Neighbors (KNN), decision tree, linear discriminant, and Naive Bayes algorithms. The next subsections are going to present a brief description of the mathematical foundations of these algorithms.

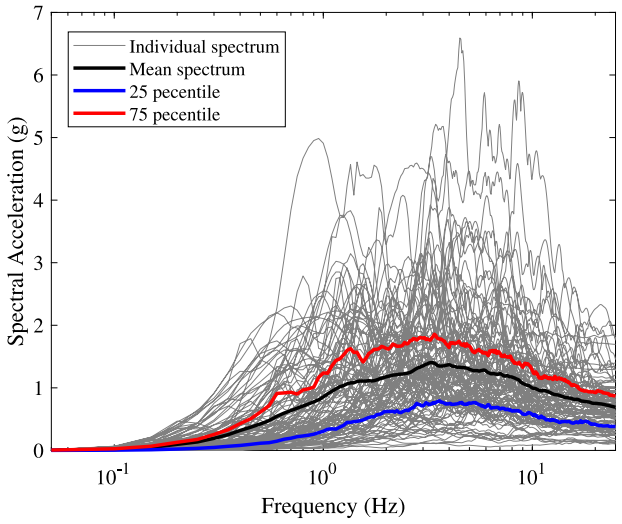

Fig. 9. Response spectra for the set of earthquake motions.

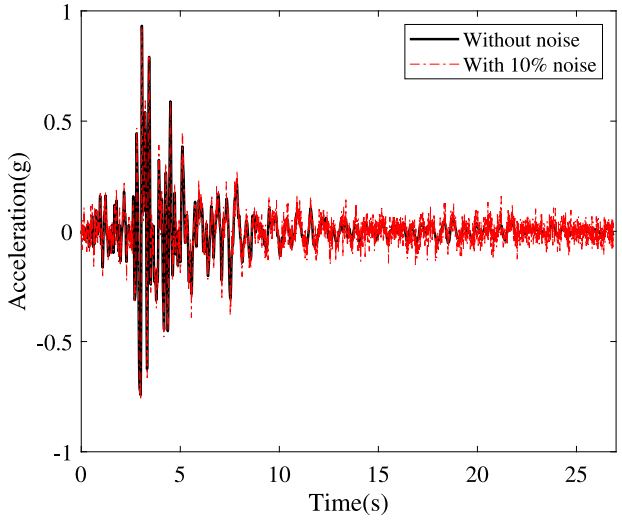

Fig. 10. Effect of 10% noise on the structural response.

4.1. Support Vector Machine (SVM)

SVM is a non-probabilistic binary classification learner. Typically, SVMs enlarge the features space by applying effective calculations through different nonlinear kernel functions. This statistical learner is typically developed for binary classification at which each observation is labeled as $y_i \in \{-1, 1\}$. The optimization problem in SVM can be written as below:

$$\underset{\omega,\beta}{min}\frac{1}{2}\|\omega\|^2 + \gamma\lambda \sum_{y_i \in C^+} B_i\xi_i + \lambda \sum_{y_i \in C^-} B_i\xi_i \tag{13}$$

$$subjected \quad to: \tag{14}$$

$$\xi_i \geq 0, \quad ; \; y_i\left[h(x_i)^T\omega + \beta\right] \geq 1 - \xi_i \quad \forall i; \tag{15}$$

where ω is the set of weights, β is the bias parameter, and ξ is the slack variable utilized to model a soft-margin classifier. Slack variables are useful to construct a generalized decision boundary by permitting some error near the boundaries. λ is the box constraint used to make a balance between the generalization and training accuracy. To train a classifier that performs better for observations with higher probability of occurrence (P_i), B_i is defined as follow:

$$B_i = \frac{P_i}{\sum_{i=1}^{m} P_i} \tag{16}$$

In order to quantify the misclassification cost, γ is defined. The misclassification penalty will increase for positive class by increasing the value of hyperparameter γ. This parameter is used to establish a uniform distribution for different labels [60].

Table 4
Distance measures proposed for W-KNN.

Distance measure	Formula
Euclidean	$D_{Euclidean} = \sqrt{\sum_{i=1}^{n}(a_i - b_i)^2}$
Minkowski	$D_{Minkowski} = (\sum_{i=1}^{n}\|a_i - b_i\|^c)^{\frac{1}{c}}$
Manhattan	$D_{Manhattan} = \sum_{i=1}^{n}\|a_i - b_i\|$
Chebyshev	$D_{Chebyshev} = \lim_{c\to\infty}(\sum_{i=1}^{n}\|a_i - b_i\|^c)^{\frac{1}{c}}$
Mahalanobis	$D_{Mahalanobis} = \sqrt{(\vec{a} - \vec{b})^T S(\vec{a} - \vec{b})}$
Cosine	$D_{Cosine} = \frac{\vec{a}.\vec{b}}{\|\vec{a}\|\|\vec{b}\|}$

4.2. K-Nearest Neighbors (KNN)

KNN is a non-parametric algorithm developed for the classification and regression [61,62]. The non-parametric term means that the algorithm does not consider any pre-defined assumption on the underlying data. This algorithm consists of two steps: (1) finding a group of KNN for a given dataset using different distance metrics, and (2) labeling the query based on the dominant class in KNN. Supposing the training set $\{(x_i, y_i)\}_{i=1}^{n}$ in which, x_i is a z-dimensional vector and y_i is the corresponding label, for a query x_j, the algorithm determines its unknown y_j as follows:

- Compute the distance between x_j and each x_i in the dataset
- Arrange the calculated distances in descending order
- Select K samples that have the nearest distance to x_j
- The label of x_j is assigned based on the majority classes of the KNNs

The Weighted-KNN (W-KNN) is an extension of KNN, which assigns a weight to the neighbors based on their distance. The value of weight would be increased by decreasing the distance of the neighbors to the test query x_j. There are various types of distance and weight measures proposed for W-KNN such as Euclidean, City block, Chebyshev, Jaccard, etc. In addition, the squared inverse and inverse rules are the main weighting measures presented for KNN. Table 4 summarizes the formulation of some important distance measures defined for two hypothetical vectors $\vec{a}$ and $\vec{b}$ where S is the covariance matrix of these vectors.

4.3. Decision tree

A decision tree classifier is defined as a recursive partitioning of the paradigm space to map the observations into the target values. The learning process of decision trees is similar to the structure of a flowchart in which the uppermost node (root node) implements a test on the features. The outcome of each node is partitioned through branches and the corresponding label is determined using leaf nodes. In general, decision trees are categorized as (1) classification trees, and (2) regression trees. In the former one, the set of features are labeled as the finite number of classes they belong to it. However, the samples are labeled as arbitrary real numbers in the regression trees. Detailed information on the regression trees is neglected because the present study is focused on the classification learners. The main issue in providing a classification tree is selecting the most effective feature

Table 5
Different splitting criteria proposed for decision tree algorithms.

Splitting criteria	Formula
Entropy	$E(X) = -\sum_{j=1}^{k} p_j \log_2(p_j)$ define $\log_2(0) = 0$
Gini index	$G(X) = \sum_{j=1}^{k} p_j(1-p_j) = 1 - \sum_{j=1}^{k} p_j^2$
Towing rule	$\Phi(X) = \frac{P_L P_R}{4}\left[\sum_{j=1}^{k}\left\lvert P(c_j\lvert A_L) - P(c_j\lvert A_R)\right\rvert\right]^2$
Deviance	$D(x_i) = -2\sum_j^k x_{ij}\log p_j$

for partitioning the samples at each node. Several splitting criteria were introduced during development of decision trees, e.g. towing rule, deviance, Gini index, and entropy [63]. Table 5 summarizes some common attribute selection criteria proposed for different decision tree algorithms. In a binary classification tree, at a given node A, there are N-point, K-class dataset. This node splits dataset to A_R and A_L (right and left nodes) with a proportion of P_R and P_L for the right and left branches, respectively. The outcome of each node labeled by K class labels, $\{c_i, \dots, c_k\}$. The probability of the sample X is calculated as $p(X = c_j) = p_j$, in which $j = 1, 2, \dots, k$ and $\sum_{j=1}^{k} p_j = 1$. In this Table, the minimum value of the entropy is 0 and occurs when one of $p_j = 1$ $(j = 1, 2, \dots, k)$. This means that all other p_j are equal to 0 [64] The minimum value of Gini index is equal to 0. This minimum value will occur if all samples in the node be of a single category [65]. Notably, the towing rule is efficient for a dataset labeled by large number of various classes [66]. In the deviance measure, $x_{ij}(i = 1, \dots, n \text{ and } j = 1, \dots, k)$ is the ith observation related to the Kth-component from the random vector X. Generally, the splitting criteria designate the type of splitting that results in the maximum reduction in the a parameter called "impurity measure". The impurity measures represent the homogeneity of training examples in the child node after each partitioning [66].

Generally, the training process in decision tree learners is continued until all the samples at the subsets have a unique label. In this condition, it is being said that the tree is a "complex tree" and is overfitted on the dataset. The overfitting problem reduces the generalization of the predictive model, and the accuracy of an overfitted model is low for new data. The pruning is defined as the process of removing the branches and leaves of the tree that decreases the test accuracy of the model. Two general approaches are recommended for pruning process, (1) pre-pruning, and (2) post-pruning technique. The readers are encouraged to review [66] to achieve more information on the pruning process.

4.4. Naive Bayes

The Naive Bayes Classifier (NBC) is a supervised classification algorithm which founded based on the class conditional independence assumption [67]. For an input vector, $X = (x_1, x_2, \dots, x_n)$, the conditional probability of kth possible outcome $(C_1, C_2, \dots, C_k)$ can be defined as below:

$$P(C_k|X) = \frac{P(X|C_k)P(C_k)}{P(X)} \tag{17}$$

the denominator $P(X)$ is as follow:

$$P(X) = \sum_{j=1}^{k}(P(C_j)\prod_{i=1}^{n} P(x_i|C_j)) \tag{18}$$

the following equation can be written by assuming that all factors in X are conditionally independent:

$$P(X|C_k) = \prod_{i=1}^{n} P(x_i|C_k) \tag{19}$$

the following equation is derived by substituting Eq. (19) and (18) into Eq. (17):

$$P(C_k|X) = \frac{\prod_{i=1}^{n} P(x_i|C_k)P(C_k)}{\sum_{j=1}^{k}(P(C_j)\prod_{i=1}^{n} P(x_i|C_j))} \tag{20}$$

finally, the NBC uses the Maximum A Posteriori (MAP) decision rule [68] to determine the class for each sample. Therefore, the NBC classifier is a function that assigns a class label $\hat{y} = C_k$ to a set of k observations as below:

$$argmax_{k\in(1,\dots,K)} = \frac{\prod_{i=1}^{n} P(x_i|c_k)P(c_k)}{P(x)} \tag{21}$$

despite the simplified assumptions that laid at the foundation of the NBC, several studies are reported surprising effectiveness of this algorithm even with strong dependencies [67].

4.5. Linear Discriminant Analysis (LDA)

The discriminant analysis is a linear combination of the features to reduce the size of feature's space and scale the features according to their importance [69]. Many feature extraction techniques apply linear transformations on the original vector of patterns to achieve new vectors with lower dimension. The main objective of Linear Discriminant Analysis (LDA) is to search a vector from the vectors space that presents better separation between different classes of data. The separability of each vector can be examined by projecting the original set of data onto these vectors. When the transformed data illustrate significant overlap, the LDA algorithm seeks a better separation by using a transformation rule know as Fisher ratio [70]. The fisher ratio for a binary problem is defined as below:

$$F_R = \frac{(\mu_1 - \mu_2)^2}{\sigma_1^2 + \sigma_2^2} = \frac{S_B}{S_W} \tag{22}$$

where μ_1 and μ_2 are the mean or center points of the first and second classes, respectively. It is obvious that $\mu_1 - \mu_2$ represents the distance between the centroids of two classes. σ_1 and σ_2 are also the variance of the first and second classes, respectively. Thus, the LDA tries to maximize the distance between two classes by maximizing the Fisher ratio. In other words, it maximizes the scatter between two classes (S_B) while making two classes as condense as possible by minimizing within class scatter (S_W). To meet this goal, a transformation vector w is applied as below:

$$F_R(w) = \frac{w^T S_B w}{w^T S_W w} \tag{23}$$

finally, the algorithm is intended to find a transformation vector w that maximizes the Fisher ratio. By differentiating $F_R(w)$ in terms of w, the following eigen value problem will obtain:

$$S_w^{-1} S_B w = \lambda w \qquad where \quad \lambda = F_R(w) = scalar \tag{24}$$

solving the eigen value problem yields:

$$w = \arg\max_w F_R(w) = S_w^{-1}(\mu_1 - \mu_2) \tag{25}$$

after projecting the feature's space onto the projection vector, a Gaussian distribution can be fitted on each class to conduct the classification problem.

5. Implementation

So far, the mathematical foundation of the proposed framework is discussed. For better understanding, this section presents an overall view of the proposed approach.

5.1. Input excitations

In order to provide a generalized dataset, a suite of 111 pair motions (Table A.1), originally developed for the SAC project [41], are employed. These motions are uniformly scaled to 16 different Peak Ground Acceleration values (PGAs), ranging from 0.05 g to 1.5 g, to generate a wide range of severity for the input excitations. Notably, the SAC motions include a set of far-field, near-field, and simulated records

representing a wide range of frequency contents. Therefore, the set of ground motions provide a generalized set of structural response for the classification problem. Fig. 9 illustrates the PGA-normalized elastic acceleration response spectra with 5% damping ratio for the suite of ground motions.

5.2. Effect of noise

It is well understood that the sensory data are accompanied by unwanted noise. The effect of noisy structural response on the learning process was considered by adding white Gaussian noise to the acceleration signals acquired from each floor of the buildings. The coefficient of signal-to-noise ratio is defined to measure the level of noise that is added to the signals. This coefficient is written as below:

$$SNR = \frac{\sigma^2_{signal}}{\sigma^2_{noise}} \tag{26}$$

where σ^2_{signal} and σ^2_{noise} are the variance of the signal and noise, respectively. Random noise is generated through the Gaussian process with a variance of $\frac{\sigma^2_{signal}}{SNR}$ and added to the clean signals acquired from the response history analysis to simulate the field condition. In this study, a maximum level of 10% noise is considered as the worst case. Fig. 10 shows the effect of 10% on the original acceleration response of the structure.

5.3. Feature extraction and labeling

After simulating the field condition by adding natural noise to the structural response, a finite number of features should be extracted from these raw acceleration histories to feed the classification learners. In this regard, all the acceleration records were de-noised using the wavelet de-noising approach explained in Section 3.6. Then, all the damage features were extracted from the acceleration signals as discussed in Section 3. The performance level of the shear wall is determined based on the recommendation of ASCE 41-17 [71] (Table A.2) to assign the proper label for each sample. According to ASCE 41-17, the performance level of a shear wall with specific design properties and construction type is determined based on the amount of plastic rotation that occurred in the body of the wall. Readers are encouraged to review Table A.2 for detailed information on the way of determining the performance metrics. After determining the extent of damage of the shear walls, the IO, LS, and CP performance levels were labeled as 0, 1, and 2, respectively.

5.4. Hyperparameter optimization

An important problem in training a classifier is selecting optimum hyperparameters to achieve the minimum cost for predictive model. To prevent the over-fitting of the classification learner, the K-fold cross-validation approach is employed. This method randomly divides the dataset into K equal parts in which $(K-1)$ partitions are utilized for training process, and the rest is considered to investigate the validity of the training algorithm. This process is iterated until all partitions are considered at least one time as the validation part. Finally, the average loss for these k trained models is reported as the cross-validation error.

$$CV_{error} = \sum_{i=1}^{K} e_k \tag{27}$$

Where CV_{error} is the cross-validation error, and e_k represent the value of error obtained for each fold. Bayesian Optimization (BO) algorithm conducts the classifier to achieve a model with minimum CV_{error}. To this end, the CV_{error} is considered as an objective function for the optimization problem. The value of CV_{error} is calculated through a Gaussian process as follow:

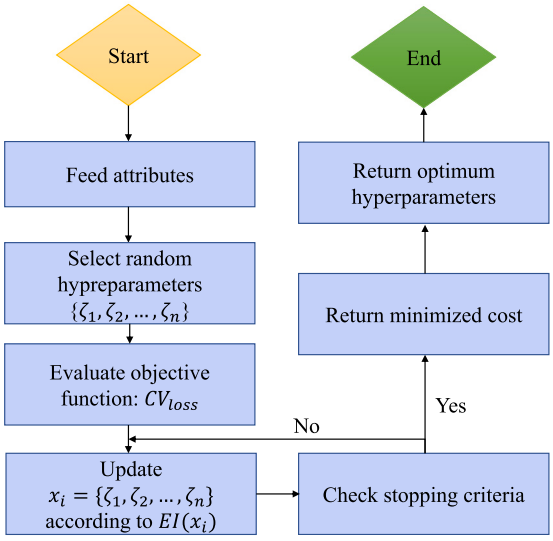

Fig. 11. Bayesian optimization algorithm.

$$CV_{error} \sim GP(M, \sum + \sigma^2 I) \tag{28}$$

where M is the average value of the Gaussian process with an initial value of 0. $\sum$ is the covariance matrix calculated from the squared exponential kernel function [72]. I is an identity matrix with compatible dimensionality. It is assumed that a Gaussian noise with a variance of σ^2 is added to the observations. To evaluate and update the hyperparameters, BO maximizes the following acquisition function:

$$EI(x) = E[max(0, \mu(z_{best}) - CV_{error})] \tag{29}$$

where z_{best} is the location of the minimum posterior's mean, and $\mu(z_{best})$ is the minimum value of the posterior's average. BO may stop after satisfying each of the following assumptions: (1) a threshold value for the number of iterations, (2) a threshold for the learning time, and (3) a specific stopping criterion that applied to the algorithm. In the present research, the stopping criterion was a threshold value for the number of iterations. This value was chosen based on the complexity of the under-study problem. Readers are referred to study [48,72] for detailed information on employing the BO algorithm for hyperparameter selection in the classification learners. Fig. 11 illustrates the BO flowchart for calculating the optimized hyperparameters.

5.5. Training procedure

A parametric study is implemented to determine the most reliable classification learner for mapping the feature's space onto the damage scenarios of the shear wall buildings. BO algorithm is used to tune the hyperparameters of each model. Besides, K-fold cross-validation technique is considered to prevent the over-fitting problem during the training process. For this purpose, the training set is partitioned into 10 equal subset. The feature's space is fed to the classification learners in the following form:

$$O^k_{i,j-x} = \left[f^1_{i,j-x}, f^2_{i,j-x}, \dots, f^6_{i,j-x}, f^7_{i,n-x}\right] \ and \tag{30}$$

$$O^k_{i,j-y} = \left[f^1_{i,j-y}, f^2_{i,j-y}, \dots, f^6_{i,j-y}, f^7_{i,n-y}\right] \tag{31}$$

where f represents the feature, i is the observation number, $j = \{1, 2, \dots, n\}$ is the story number, and k is the number of features. As mentioned before, the correlation feature is only determined for the roof level. Therefore, $f^7_{i,n-x}$ and $f^7_{i,n-y}$ are the correlation features

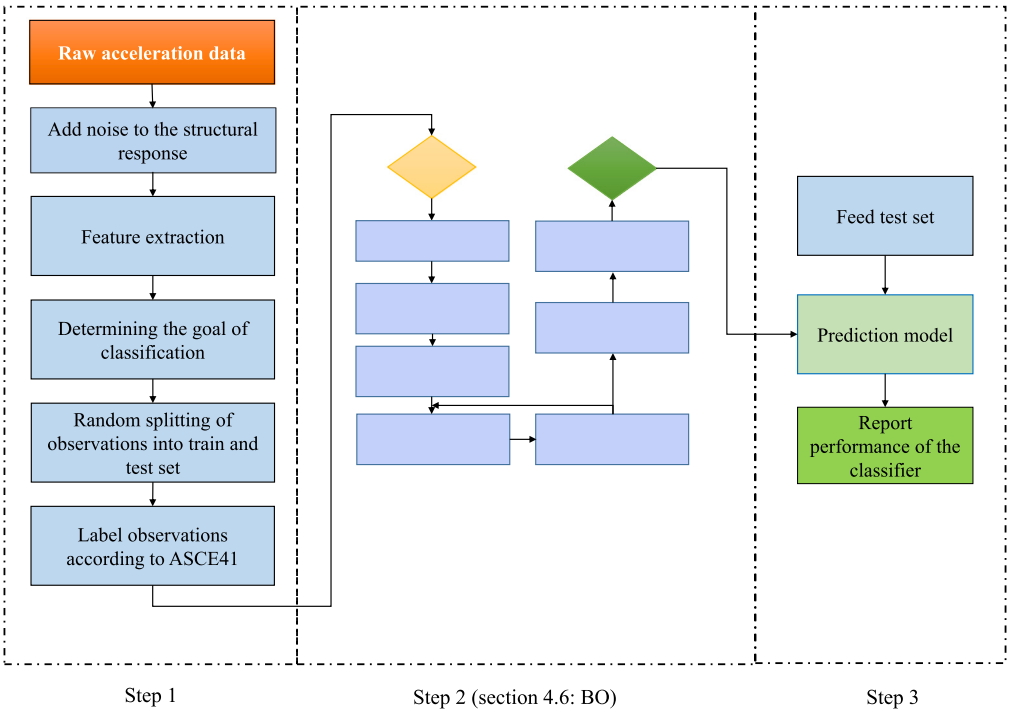

Fig. 12. Outline of the proposed framework.

Table 6
Comparison between the performance of different models.

Learning algorithm	7-story building	9-story building	13-story building	Average
Decision tree	93%	83.5%	94.9%	90.5%
Linear discriminant	93.4%	85.6%	92.9%	90.6
Naive Bayes	87.4%	83.7%	90.6%	87.2%
SVM	94.6%	89.3%	95.4%	93.1%
KNN	95.7%	89.7%	95.6%	93.6%

obtained for the roof level of each building in x and y directions, receptively. Notably, the dataset is randomly shuffled, and 80% of the examples are employed for training process. Besides, the remaining bin is utilized to test the accuracy of the trained classifier. Fig. 12 shows the general view of the proposed algorithm.

A parametric study was performed to obtain a sufficient number of features that should be used for achieving a predictive model with maximum accuracy and minimum computational cost. According to this investigation, it is concluded that 4 of the proposed features improve the accuracy of the classification learner. Therefore, in addition to tuning the classifier hyperparameters, another problem that should be solved during the BO algorithm is selecting four of the more significant features among the seven attributes proposed in this study.

6. Results

This section first describes the results of different classifiers in detecting the structural damage for the mentioned case study buildings. Then, by selecting the best classifier, the results of this model are explained in detail to assess the efficiency of the presented approach in estimating the damage level of concrete shear wall buildings under earthquake motions.

6.1. Performance of different classifiers

As mentioned before, a parametric study is carried out to determine the best learner for solving the under-study classification problem. For this purpose, the score of different models was considered as the performance metric. Table 6 summarizes the average accuracy of each model in detecting the performance level of various stories of the buildings. According to this table, the KNN algorithm performs better than the other classification learners in terms of cross-validation accuracy. Of course, the SVM algorithm demonstrates comparable accuracy to the KNN, but the optimization process of SVM shows more computational cost. On the other hand, the Naive Bayes algorithm, with an average cross-validation accuracy of 87.2%, was the worst case in learning the damage detection problem. As a result, the KNN algorithm is proposed to identify the extent of damage in concrete shear wall buildings. In the following subsections, the results of the KNN algorithm in detecting the performance level of each case study model are explained. The confusion matrix calculated for the test set, the Receiver Operating Characteristic (ROC) curve, and the cross-validation accuracy of each classifier are presented to evaluate the performance of the predictive models in a perceptible manner. A confusion matrix represents the robustness of the model in terms of the true predicted instances against the false classified samples. In addition, a ROC curve presents the True Positive Rate (TPR) versus the False Positive Rate (FPR) along the training process for different thresholds. Readers can refer to Fan et al. [73] to obtain more information on the ROC curve characteristics. Whatever the ROC curve is closer to the upper-left corner of the plot, the prediction model presents more accuracy and generalization. The area under the curve (AUC) is defined to measure the closeness of the ROC curve to the upper-left corner. It is obvious that an AUC closer to 1 indicates a more reliable prediction model with a higher estimation accuracy. This index is more applicable when the dataset is polluted to noise. On average, the number of optimized neighbors is selected as 11 for all stories of the structure. Moreover, *Mahalanobis* distance and *squared inverse* rule were respectively selected as the most efficient

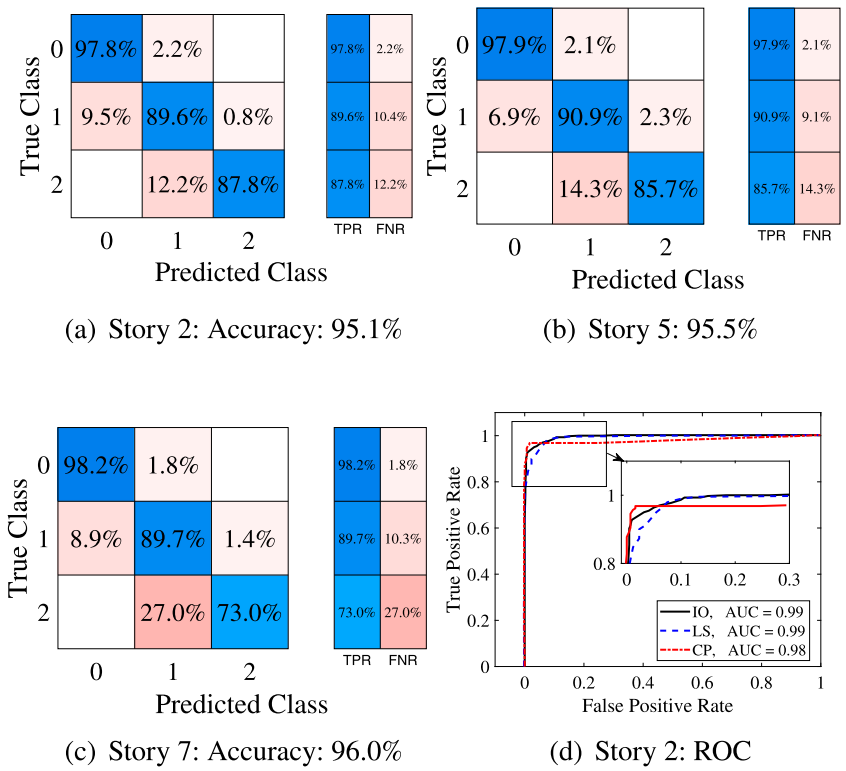

Fig. 13. The ROC curve and confusion matrices for damage extent detection of the 7-story building.

distance metric and weighting measure during the BO algorithm. It should be mentioned that the *Drift*, *Correlation*, and *MCAV* attributes were chosen as the optimized features among the seven pre-defined damage indicators. Fig. 13 shows the confusion matrices for different floors of the seven-story building. A close look to this figure reveals that the proposed method provides promising accuracy in estimating the local damage exposed to the shear walls of the building. A mean accuracy of 95.6% is achieved for estimating the performance level of each floor. The ROC curve that is presented in Fig. 13(d) belongs to the story level with minimum cross-validation accuracy (second story). The minimum AUC among different performance levels was 0.96, which represents the effectiveness of the selected features in estimating the damage state of the floors. The prediction model illustrates the minimum true positive rate of 73.0% for the last floor. Notably, the false negative rate in this story can be assigned to the proximity of those portions of samples to the true predicted boundaries, and also the low number of samples exceed the LS level in the last floor of the building. Hence, the false estimated cases do not remarkably influence decision-making metrics for the confronting actions after the earthquake. In addition, since the prediction models determine the performance level of the building for each story, a reliable decision can be made for the whole building.

Fig. 14 illustrates the confusion matrices for shear walls in X direction of the nine-story building. On average, the accuracy of the prediction models was equal to 91.5% for identifying the extent of damage in X direction. Fig. 14(d) shows the ROC curve of the classification learner for the story with minimum prediction accuracy (second story). According to this figure, The AUC values are close to 1.0, which indicates the generalization and robustness of the proposed classification process. The minimum true positive rate for different performance levels through all the stories was 75.7% for the shear walls in X direction. Accordingly, the false negative rate in that story was 24.3%. As the features presented in this study are directly related to the structural damage of the building, this rate of false predicted cases can be specified to the vicinity of these portions of instances to the true predicted borders. Thus, the false predicted cases do not significantly influence the decision-making process after the event. Moreover, expert engineers can make a reliable decision for the whole structure by considering the performance levels achieved for each story of the structure.

Fig. 15 shows the confusion matrices for shear walls in the Y direction of the building. The average accuracy of the classifiers was 89.4% for identifying the extent of damage in the Y direction. It is obvious that the average accuracy of the prediction models is less than the seven-story for both directions. This problem is due to the complex behavior of the nine-story building compared to the seven-story case because the intense vertical irregularity exists in the architecture of the nine-story building. Fig. 15(d) illustrates the ROC curve of the prediction model for the second story of the building, which presents the minimum prediction accuracy among all the stories of the structure. A closer look at this figure reveals that all the AUC values are greater than 0.94, which demonstrates the promising accuracy of the models in identifying the severity of damage for each floors of the building. These figures indicate that the proposed method capable of estimating the damage state of the concrete shear walls of the building with an average accuracy of 89.4%. This means that the prediction models may represent an average false prediction rate of 11.6% for marginal cases. However, these false prediction cases have similar damage indicators to the proximate performance level. Therefore, these false classified scenarios generally do not impose significant errors on the decision-making metrics.

Fig. 16 reveals the confusion matrices for shear walls in X direction of the thirteen-story building. An average accuracy of 91.4% was obtained for detecting the extent of damage in X-direction shear walls. As an example, Fig. 16(d) illustrates the ROC curve of the prediction model for the third story (story with minimum cross-validation accuracy). This figure indicates that the AUC values are close to 1.0 for all the performance levels. It can be concluded that the prediction models presents promising performance in estimating the level of damage. The minimum true positive rate belongs to the CP state of the last story

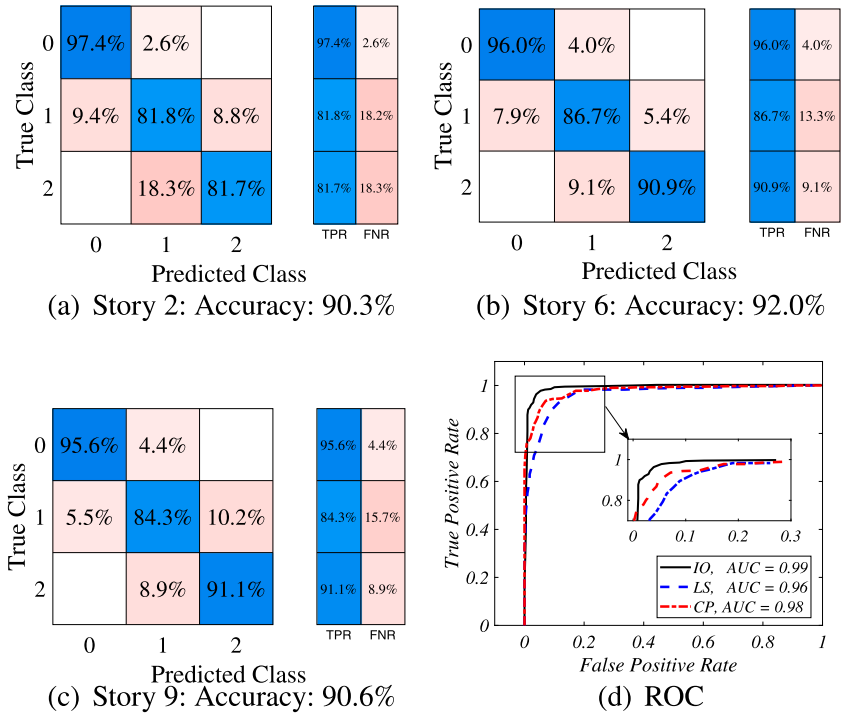

Fig. 14. The ROC curve and confusion matrices for damage detection model of the 9-story building (Shear walls in X direction).

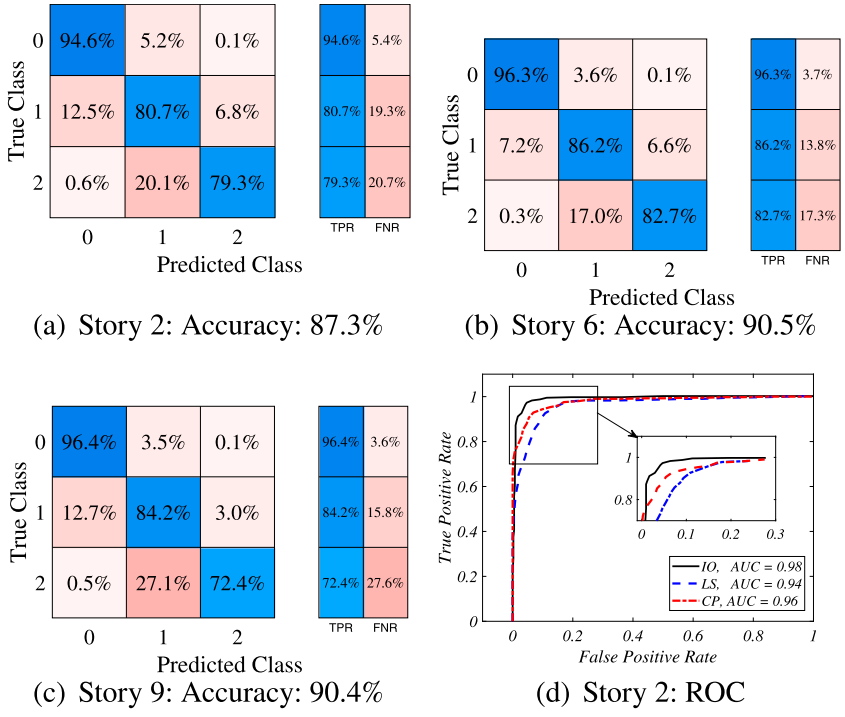

Fig. 15. The ROC curve and confusion matrices for damage detection model of the 9-story building (Shear walls in Y direction).

which was equal to 68.8%. It is obvious from Fig. 16(c) that the predictive model underestimates the extent of damage in 31.2% of cases. However, approximately in 29.5% of cases, the false predicted cases do not significantly affect the decision-making process because these false predicted samples have marginal damage indicators between two adjacent classes. The lowest level of performance for the CP damage state was related to the low number of samples that exceeded the LS level in the last story of the building. This behavior was predictable taking into account the fundamental concepts of dynamics of structures. It should be mentioned that expert engineers can also make their decision considering the damage state obtained for adjacent floors of the building.

Similarly, Fig. 17 summarizes the confusion matrices for the shear walls in Y-direction of the thirteen-story building. The overall view of this figure reveals the efficiency of the proposed framework in estimating the structural damage subjected to the concrete shear wall buildings. Similar to the X-direction, an average accuracy of 91.4% was achieved for prediction models of the shear walls in the Y direction.

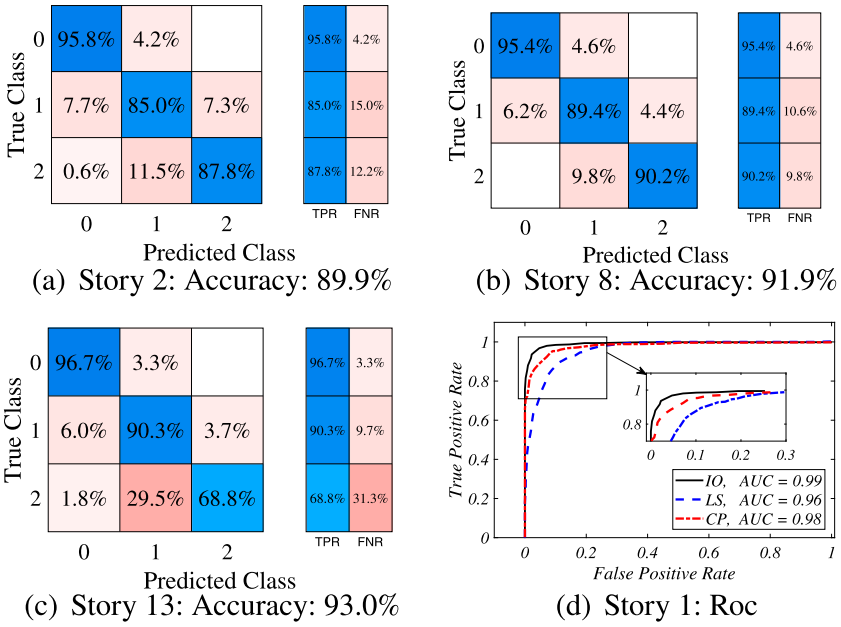

Fig. 16. The ROC curve and confusion matrices for damage detection model of the 13-story building (Shear walls in X direction).

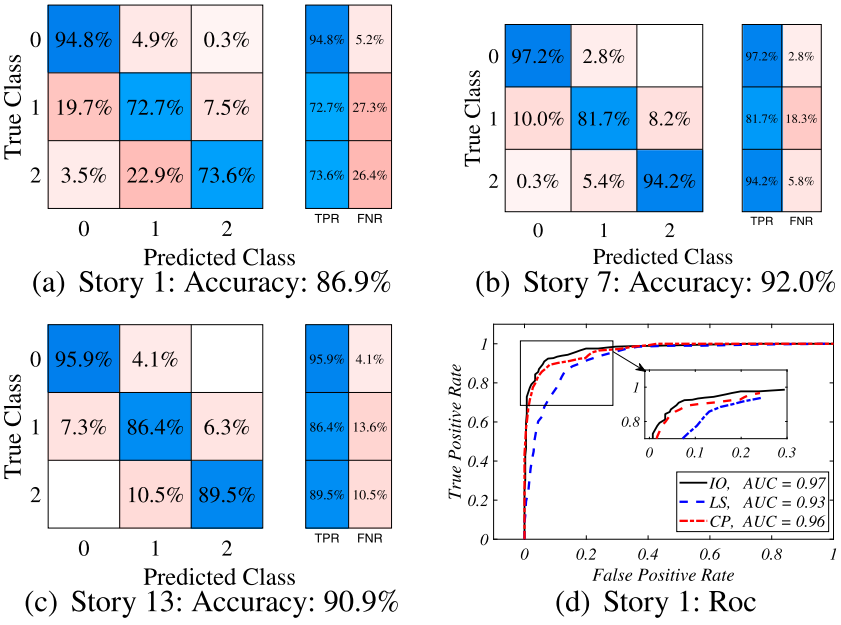

Fig. 17. The ROC curve and confusion matrices for damage detection model of the 13-story building (Shear walls in Y direction)

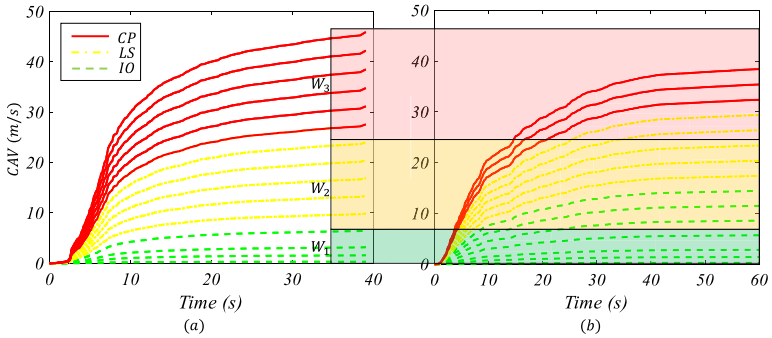

Fig. 18. Comparison between the CAV obtained for two different ground motions.

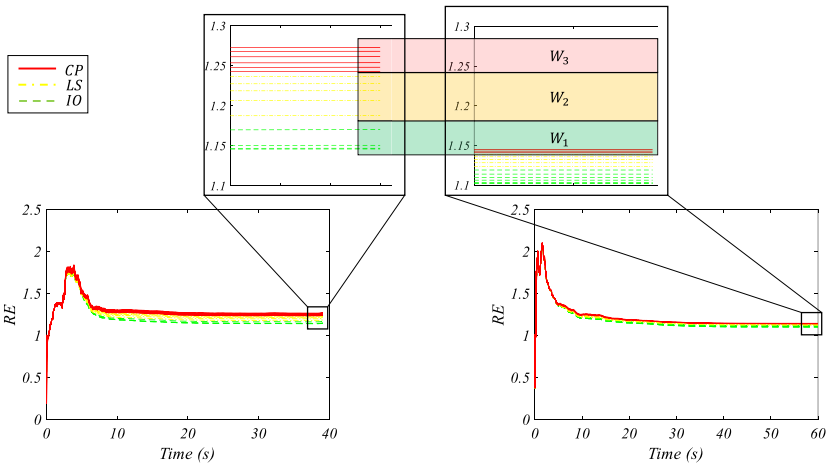

Fig. 19. Comparison between the RE obtained for two different ground motions.

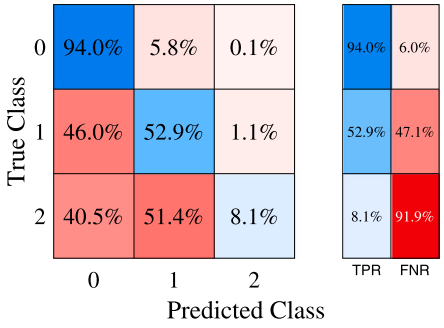

Fig. 20. Predictive model based on CAV and RE attributes.

According to Fig. 17(d), the ROC curves of the story with minimum cross-validation accuracy are close to the upper-left corner of the diagram and their AUC is close to 1. Therefore, the prediction models perform acceptably even for the worst prediction model. Fig. 17(a) indicates that the prediction model of this story underestimates the LS state in 19.7% and overestimates them in 7.5% of cases. In addition, this predictive model underestimates the CP state in 26.4% of cases. Of course, approximately 22.9% of these underestimated cases belong to those samples that have similar damage indicators to the LS state. In fact, these scenarios do not impose much error on the decision-making metrics as they are in the margins of the acceptance criterion defined in $ASCE-41$.

6.2. Discussion

This research investigated the efficiency of two commonly used damage indicators proposed for identifying the extent of damage in concrete shear walls buildings. Many studies showed the efficiency of energy-based damage indicators, such as output energy and the relative energy between the output and input signals of the structure, for detecting the structural damage in buildings [29,31,32]. However, based on an investigation conducted in the present study, it is shown that these features are not capable of classifying the severity of local damage subjected to the concrete shear wall frames under ground motions. Fig. 18 illustrates the CAV diagrams for two records ($CoyoteLake$ and $MorganHill$) with different durations, where both motions scaled similarly. This figure indicates that the maximum value of CAV is dependent on the ground motion duration. In this figure, the CAV response space was partitioned into three windows of $W1$, $W2$, and $W3$ based on the performance level of the building under the $CoyoteLake$ earthquake. Despite the good agreement between the CAV and damage extent in each event, the damage extents obtained from two records have interfered. The same behavior was observed for the energy ratio feature (Fig. 19). To illustrate the total efficiency of these two features in detecting the severity of damage at concrete shear wall buildings, a KNN classifier was trained, and an example confusion matrix of this process is shown in Fig. 20. The total accuracy of 69% achieved for the prediction model indicates the insufficiency of these damage indicators for identifying the local damage subjected to the concrete shear walls. According to this study, it can be concluded that the extent of damage has a direct relation to the lateral behavior of the building system, and the damage indicators proposed for a specified building may not be effective for another structural system.

7. Conclusion

This paper presented a rapid algorithm for identifying the severity of local damage in the concrete shear wall buildings. A total number of 1884 nonlinear response history analyses were conducted for each building using the SAC motions. A suite of damage indicators was extracted from the acceleration signals to construct the prediction models. A parametric study was carried out to determine the most efficient learner for classifying the damage states of the buildings. The KNN classifier was selected to construct the predictive models because of its maximum accuracy compared to the other algorithms. The Bayesian optimization algorithm implemented to tune the hyperparameters of the classification learners. The main conclusions derived from the study are as below:

- The proposed features were efficient in detecting the probable extent of local damage subjected to the concrete shear walls.
- The parametric study showed that the KNN classifier is the most reliable algorithm for identifying the structural damage at the concrete shear wall buildings.
- Bayesian optimization algorithm prevented the possible errors related to the improper architecture of the classification learner.
- According to the outcome of the Bayesian optimization, it was concluded that the $Drift$, $Correlation$, and $MCAV$ are the most powerful indicators in classifying the damage states of the concrete shear wall buildings.
- Results showed that vertical irregularity could decrease the accuracy of the prediction models because of the more complex dynamic behavior of such buildings.
- The task of damage identification was successfully implemented by achieving an average accuracy of 95.6%, 90.4%, and 91.4% for 7-, 9-, and 13-story buildings, respectively.

Table A.1
SAC ground motions.

ID	Event name	Duration (s)	PGA (g)	ID	Event name	Duration (s)	PGA (g)
1	CoyoteLake	26.86	0.59	56	LongBeach	39.1	0.174
2	ImperialValley	39.1	0.143	57	MorganHill	60	0.663
3	Kernmodified	78.62	0.159	58	WestWashington	80	0.384
4	Landersm	80	0.338	59	WestWashington	66.7	0.389
5	MorganHill	60	0.546	60	NorthPalm	60	0.588
6	Parkfield	43.94	0.781	61	PugetSound	81.84	0.752
7	Parkfield	26.16	0.79	62	PugetSound	74.1	0.369
8	NorthPalm	60	0.518	63	EasternWa	60	0.575
9	SanFernando	79.48	0.253	64	Llolleom	100	0.698
10	Whittier	40	0.769	65	Vinadel Mar	100	0.542
11	ImperialValley	53.48	0.676	66	Mendocino	60	0.756
12	ImperialValley	39.4	0.488	67	Erzincan	20.78	0.605
13	ImperialValley	39.1	0.302	68	Olympiamod	80	0.896
14	Landersmod	80	0.426	69	Seattlemod	81.84	1.756
15	Landersmod	80	0.52	70	Valpariso	100	1.637
16	LomaPrieta	40	0.97	71	Valpariso	100	1.271
17	Northridge	60	0.678	72	DeepInterplate	80	0.797
18	Northridge	14.96	0.58	73	Miyagioki	80	0.784
19	Northridge	60	0.817	74	ShallowInter	80	0.563
20	NorthPalm	60	1.019	75	ShallowInter	80	0.75
21	Kobemodi	60	1.283	76	Tabasmod	50	0.978
22	lomaPrieta	25	0.473	77	LomaPrieta	25	0.718
23	Northridge	14.96	0.944	78	LomaPrieta	40	0.686
24	Northridge	60	1.33	79	CMendocino	60	0.655
25	Tabasmod	50	0.992	80	Erzincan	20.78	0.457
26	ElysianPark	30	1.296	81	Landersmod	49.3	0.799
27	ElysianPark	30	0.782	82	Nothridge	14.98	0.89
28	ElysianPark	30	1.101	83	Nothridge	60.02	0.732
29	PalosVerdes	60	0.776	84	Kobemodi	60	1.088
30	PalosVerdes	60	0.625	85	Kobemodi	40.1	0.786
31	hangingwall	30	0.124	86	Elysianmod	40	0.892
32	footwall	30	0.144	87	Elysianmod	40	1.803
33	NewHampshire	19.24	0.576	88	Elysianmod	40	1.013
34	Nahannimod	20.34	0.088	89	Elysianmod	40	0.922
35	Nahannimod	18.76	0.074	90	Elysianmod	40	1.162
36	Nahannimod	19.02	0.136	91	Palosmod	80	0.974
37	Saguenay	17.74	0.29	94	Palosmod	80	0.968
38	Saguenay	29.58	0.524	95	PalosVerdes	80	0.874
39	Saguenay	39.06	0.227	96	PalosVerdes	80	0.793
40	Saguenay	33.26	0.273	97	PalosVerdes	80	0.916
41	footwall	30	0.316	98	Northridge,CA	30	0.516
42	footwall	30	0.335	99	Northridge,CA	20	0.482
43	footwall	30	0.309	100	Duzce,Turkey	55.9	0.822
44	Nahannimod	20.34	0.252	101	HectorMine,CA	45.32	0.337
45	Nahannimod	18.76	0.211	102	ImperialValley	99.92	0.351
46	Nahannimod	19.02	0.389	103	ImperialValley	39.04	0.38
47	Saguenay	17.74	0.783	104	Kobe,Japan	40.96	0.509
48	Saguenay	29.58	1.504	105	Kobe,Japan	40.96	0.243
49	Saguenay	39.06	0.651	106	Kocaeli,Turkey	27.2	0.358
50	Saguenay	33.26	0.781	107	Kocaeli,Turkey	30	0.219
51	Landers,CA	27.98	0.417	108	Chi-Chi,Taiwan	61.78	0.44
52	LomaPrieta,CA	39.96	0.541	109	Chi-Chi,Taiwan	53.66	0.512
53	LomaPrieta,CA	39.96	0.555	110	SanFernando	28	0.21
54	Manjil,Iran	46	0.538	111	Friuli,Italy	36.36	0.351
55	SuperHills,CA	40	0.358				

Table A.2
Modeling parameters and numerical acceptance criteria for nonlinear procedures—reinforced concrete structural walls.

Conditions			Acceptable plastic hinge rotation (Radians)		
			Performance level		
			IO	LS	CP
$\frac{(A_s - A'_s)f_{yE} + P}{t_w I_w f'_{cE}}$	$\frac{V}{t_w I_w \sqrt{f'_{cE}}}$	Confined Boundary			
≤ 0.1	≤ 4	Yes	0.005	0.015	0.020
≤ 0.1	≥ 6	Yes	0.004	0.010	0.015
≥ 0.25	≤ 4	Yes	0.003	0.009	0.012
≥ 0.25	≥ 6	Yes	0.0015	0.005	0.010
≤ 0.1	≤ 4	No	0.002	0.008	0.015
≤ 0.1	≥ 6	No	0.002	0.006	0.010
≥ 0.25	≤ 4	No	0.001	0.003	0.005
≥ 0.25	≥ 6	No	0.001	0.002	0.004

- This research illustrates that the efficiency of damage indicators depends on the lateral behavior of the building. For example, several studies show that damage indexes like output energy of the structure and relative energy between the output and input signals are efficient in determining the damage level in structures. However, this study reveals that these features are not suitable for achieving a reliable local-damage detection framework in reinforced concrete shear wall buildings.
- The proposed method did not consider the uncertainties related to the ground motion directionality, material properties, etc. These uncertainties can be applied to the framework to analyze the reliability of the proposed technique [21,74].

Declaration of competing interest

The authors declare that they have no known competing financial interests or personal relationships that could have appeared to influence the work reported in this paper.

Appendix

See Tables A.1 and A.2

References

[1] Azimi M, Pekcan G. Structural health monitoring using extremely compressed data through deep learning. Comput-Aided Civ Infrastruct Eng 2019. http://dx.doi.org/10.1111/mice.12517.

[2] Cha Y-J, Choi W, Büyüköztürk O. Deep learning-based crack damage detection using convolutional neural networks. Comput-Aided Civ Infrastruct Eng 2017;32(5):361–78. http://dx.doi.org/10.1111/mice.12263.

[3] Rehman SKU, Ibrahim Z, Memon SA, Jameel M. Nondestructive test methods for concrete bridges: A review. Constr Build Mater 2016;107:58–86. http://dx.doi.org/10.1016/j.conbuildmat.2015.12.011.

[4] Mirtaheri M, Salkhordeh M, Mohammadgholiha M. A system identification-based damage-detection method for gravity dams. Shock Vib 2021;2021. http://dx.doi.org/10.1155/2021/6653254.

[5] Chang PC, Flatau A, Liu S. Health monitoring of civil infrastructure. Struct Health Monit 2003;2(3):257–67. http://dx.doi.org/10.1177/1475921703036169.

[6] Karami-Mohammadi R, Mirtaheri M, Salkhordeh M, Hariri-Ardebili MA. Vibration anatomy and damage detection in power transmission towers with limited sensors. Sensors 2020;20(6):1731.

[7] Arici Y, Mosalam KM. Modal identification of bridge systems using state-space methods. Struct Control Health Monitor: Official J Int Assoc Struct Control Monitor Eur Assoc Control Struct 2005;12(3–4):381–404. http://dx.doi.org/10.1002/stc.76.

[8] Jafarkhani R, Masri SF. Finite element model updating using evolutionary strategy for damage detection. Comput-Aided Civ Infrastruct Eng 2011;26(3):207–24. http://dx.doi.org/10.1111/j.1467-8667.2010.00687.x.

[9] Farrar CR, Worden K. Structural health monitoring: A machine learning perspective. John Wiley & Sons; 2012.

[10] Ying Y, Garrett Jr JH, Oppenheim IJ, Soibelman L, Harley JB, Shi J, et al. Toward data-driven structural health monitoring: Application of machine learning and signal processing to damage detection. J Comput Civ Eng 2013;27(6):667–80. http://dx.doi.org/10.1061/(ASCE)CP.1943-5487.0000258.

[11] Tsou P, Shen M-HH. Structural damage detection and identification using neural networks. AIAA J 1994;32(1):176–83. http://dx.doi.org/10.2514/3.11964.

[12] Worden K, Manson G, Fieller NR. Damage detection using outlier analysis. J Sound Vib 2000;229(3):647–67. http://dx.doi.org/10.1006/jsvi.1999.2514.

[13] Zhao J, Ivan JN, DeWolf JT. Structural damage detection using artificial neural networks. J Infrastruct Syst 1998;4(3):93–101. http://dx.doi.org/10.1061/(ASCE)1076-0342(1998)4:3(93).

[14] Yam L, Yan Y, Jiang J. Vibration-based damage detection for composite structures using wavelet transform and neural network identification. Compos Struct 2003;60(4):403–12. http://dx.doi.org/10.1016/S0263-8223(03)00023-0.

[15] Zhang Y, Burton HV, Sun H, Shokrabadi M. A machine learning framework for assessing post-earthquake structural safety. Struct Saf 2018;72:1–16. http://dx.doi.org/10.1016/j.strusafe.2017.12.001.

[16] Sajedi SO, Liang X. Vibration-based semantic damage segmentation for large-scale structural health monitoring. Comput-Aided Civ Infrastruct Eng 2020;35(6):579–96. http://dx.doi.org/10.1111/mice.12523.

[17] Salkhordeh M, Mirtaheri M, Soroushian S. A decision-tree-based algorithm for identifying the extent of structural damage in braced-frame buildings. Struct Control Health Monit 2021;28(11):e2825. http://dx.doi.org/10.1002/stc.2825.

[18] Neves AC, Leander J, González I, Karoumi R. An approach to decision-making analysis for implementation of structural health monitoring in bridges. Struct Control Health Monit 2019;26(6):e2352. http://dx.doi.org/10.1002/stc.2352.

[19] Salkhordeh M, Alishahiha F, Mirtaheri M, Soroushian S. A rapid neural network-based demand estimation for generic buildings considering the effect of soft/weak story. Struct Infrastruct Eng 2022;1–20.

[20] Wang L, Liu Y, Li M. Time-dependent reliability-based optimization for structural-topological configuration design under convex-bounded uncertain modeling. Reliab Eng Syst Saf 2022;221:108361.

[21] Wang L, Liu Y, Liu D, Wu Z. A novel dynamic reliability-based topology optimization (DRBTO) framework for continuum structures via interval-process collocation and the first-passage theories. Comput Methods Appl Mech Engrg 2021;386:114107.

[22] Salkhordeh M, Mirtaheri M. A swift neural network-based algorithm for demand estimation in concrete moment-resisting buildings. Numer Methods Civ Eng 2021;6(3):28–36.

[23] Liu Y, Wang L, Gu K, Li M. Artificial neural network (ANN)-Bayesian probability framework (BPF) based method of dynamic force reconstruction under multi-source uncertainties. Knowl-Based Syst 2022;237:107796.

[24] Ghiasi R, Torkzadeh P, Noori M. A machine-learning approach for structural damage detection using least square support vector machine based on a new combinational kernel function. Struct Health Monit 2016;15(3):302–16. http://dx.doi.org/10.1177/1475921716639587.

[25] Ni Y, Zhou X, Ko J. Experimental investigation of seismic damage identification using PCA-compressed frequency response functions and neural networks. J Sound Vib 2006;290(1–2):242–63. http://dx.doi.org/10.1016/j.jsv.2005.03.016.

[26] De Ridder D, Duin RP. Locally linear embedding for classification. Tech. rep. PH-2002-01, Pattern Recognition Group, Dept. of Imaging Science & Technology, Delft University of Technology, Delft, the Netherlands; 2002, p. 1–12.

[27] Hyvärinen A, Oja E. Independent component analysis: Algorithms and applications. Neural Netw 2000;13(4–5):411–30. http://dx.doi.org/10.1016/S0893-6080(00)00026-5.

[28] Reed JW, Kassawara RP. A criterion for determining exceedance of the operating basis earthquake. Nucl Eng Des 1990;123(2–3):387–96. http://dx.doi.org/10.1016/0029-5493(90)90259-Z.

[29] Cabanas L, Benito B, Herráiz M. An approach to the measurement of the potential structural damage of earthquake ground motions. Earthq Eng Struct Dyn 1997;26(1):79–92. http://dx.doi.org/10.1002/(SICI)1096-9845(199701)26:1<79::AID-EQE624>3.0.CO;2-Y.

[30] Bandara RP, Chan TH, Thambiratnam DP. Structural damage detection method using frequency response functions. Struct Health Monit 2014;13(4):418–29. http://dx.doi.org/10.1177/1475921714522847.

[31] Muin S, Mosalam KM. Cumulative absolute velocity as a local damage indicator of instrumented structures. Earthq Spectra 2017;33(2):641–64. http://dx.doi.org/10.1193/090416EQS142M.

[32] Sajedi SO, Liang X. A data-driven framework for near real-time and robust damage diagnosis of building structures. Struct Control Health Monit 2019;e2488. http://dx.doi.org/10.1002/stc.2488.

[33] American Society of Civil Engineers. Seismic evaluation and retrofit of existing buildings. American Society of Civil Engineers; 2017.

[34] Avci O, Abdeljaber O, Kiranyaz S, Hussein M, Gabbouj M, Inman DJ. A review of vibration-based damage detection in civil structures: From traditional methods to machine learning and deep learning applications. Mech Syst Signal Process 2021;147:107077. http://dx.doi.org/10.1016/j.ymssp.2020.107077.

[35] Lin Y-z, Nie Z-h, Ma H-w. Structural damage detection with automatic feature-extraction through deep learning. Comput-Aided Civ Infrastruct Eng 2017;32(12):1025–46. http://dx.doi.org/10.1111/mice.12313.

[36] Zhao B, Taucer F, Rossetto T. Field investigation on the performance of building structures during the 12 May 2008 wenchuan earthquake in China. Eng Struct 2009;31(8):1707–23. http://dx.doi.org/10.1016/j.engstruct.2009.02.039.

[37] Watanabe E, Sugiura K, Nagata K, Kitane Y. Performances and damages to steel structures during the 1995 Hyogoken-Nanbu earthquake. Eng Struct 1998;20(4–6):282–90. http://dx.doi.org/10.1016/S0141-0296(97)00029-1.

[38] Massone L, Orakcal K, Wallace J. Shear-flexure interaction for structural walls. Spec Publ 2006;236:127–50.

[39] Orakcal K, Wallace JW. Flexural modeling of reinforced concrete walls-experimental verification. ACI Mater J 2006;103(2):196.

[40] Sherstobitoff J, Cajiao P, Adebar P. Repair of an 18-story shear wall building damaged in the 2010 Chile earthquake. Earthq Spectra 2012;28(1_suppl1):335–48. http://dx.doi.org/10.1193/1.4000028.

[41] Somerville PG. Development of ground motion time histories for phase 2 of the FEMA/SAC steel project. SAC Joint Venture; 1997.

[42] Yassin MHM. Nonlinear analysis of prestressed concrete structures under monotonic and cyclic loads [Ph.D. thesis], University of California, Berkeley; 1994.

[43] Committee A. Building code requirements for structural concrete (ACI 318-14) and commentary. American Concrete Institute; 2014.

[44] Saatcioglu M, Razvi SR. Strength and ductility of confined concrete. J Struct Eng 1992;118(6):1590–607. http://dx.doi.org/10.1061/(ASCE)0733-9445(1992)118:6(1590).

[45] Cando M, Hube M, Parra P, Arteta C. Effect of stiffness on the seismic performance of code-conforming reinforced concrete shear wall buildings. Eng Struct 2020;219:110724. http://dx.doi.org/10.1016/j.engstruct.2020.110724.
[46] Xie L, Lu X, Lu X, Huang Y, Ye L. Multi-layer shell element for shear walls in OpenSees. In: Computing in civil and building engineering (2014). 2014, p. 1190–7.
[47] Lu X, Xie L, Guan H, Huang Y, Lu X. A shear wall element for nonlinear seismic analysis of super-tall buildings using OpenSees. Finite Elem Anal Des 2015;98:14–25. http://dx.doi.org/10.1016/j.finel.2015.01.006.
[48] Snoek J, Larochelle H, Adams RP. Practical bayesian optimization of machine learning algorithms. In: Advances in neural information processing systems. 2012, p. 2951–9.
[49] Campbell K, Bozorgnia Y. Use of cumulative absolute velocity (CAV) in damage assessment. In: Proc. of 15th world conf. in earthquake eng. 2012, p. 1–10.
[50] ATC58. Seismic performance assessment of buildings, Vol. 1 (Methodology). California: Redwood City; 2012a.
[51] Donoho DL. Progress in wavelet analysis and WVD: A ten minute tour. Progress Wavelet Anal Appl 1993;109–28.
[52] Donoho DL, Johnstone JM. Ideal spatial adaptation by wavelet shrinkage. Biometrika 1994;81(3):425–55.
[53] Donoho DL. De-noising by soft-thresholding. IEEE Trans Inform Theory 1995;41(3):613–27.
[54] Donoho DL, Johnstone IM, Kerkyacharian G, Picard D. Wavelet shrinkage: Asymptopia? J R Stat Soc Ser B Stat Methodol 1995;57(2):301–37. http://dx.doi.org/10.1111/j.2517-6161.1995.tb02032.x.
[55] Daubechies I. Ten lectures on wavelets. SIAM; 1992.
[56] Ansari A, Noorzad A, Zare M. Application of wavelet multi-resolution analysis for correction of seismic acceleration records. J Geophys Eng 2007;4(4):362–77. http://dx.doi.org/10.1088/1742-2132/4/4/002.
[57] Soroushian S, Maragakis EM, Ansari A. Estimation of vertical floor displacement using a wavelet de-noising method. J Earthq Eng 2016;20(2):279–97. http://dx.doi.org/10.1080/13632469.2015.1085466.
[58] Brownjohn JM. Ambient vibration studies for system identification of tall buildings. Earthq Eng Struct Dyn 2003;32(1):71–95. http://dx.doi.org/10.1002/eqe.215.
[59] Newland DE. An introduction to random vibrations, spectral & wavelet analysis. Courier Corporation; 2012.
[60] Suthaharan S. Support vector machine. In: Machine learning models and algorithms for big data classification. Springer; 2016, p. 207–35.
[61] Fix E, Hodges JL. Discriminatory analysis. Nonparametric discrimination: Consistency properties. Int Stat Rev/Rev Int Stat 1989;57(3):238–47. http://dx.doi.org/10.2307/1403797.
[62] Altman NS. An introduction to kernel and nearest-neighbor nonparametric regression. Amer Statist 1992;46(3):175–85. http://dx.doi.org/10.1080/00031305.1992.10475879.
[63] Al-Hegami AS. Classical and incremental classification in data mining process. Int J Comput Sci Netw Secur 2007;7(12):179–87.
[64] Quinlan JR. Induction of decision trees. Mach Learn 1986;1(1):81–106. http://dx.doi.org/10.1023/A%3A1022643204877.
[65] Quinlan JR. C4. 5: Programs for machine learning. Elsevier; 2014.
[66] Esposito F, Malerba D, Semeraro G, Kay J. A comparative analysis of methods for pruning decision trees. IEEE Trans Pattern Anal Mach Intell 1997;19(5):476–91.
[67] Feng X, Li S, Yuan C, Zeng P, Sun Y. Prediction of slope stability using naive Bayes classifier. KSCE J Civ Eng 2018;22(3):941–50. http://dx.doi.org/10.1007/s12205-018-1337-3.
[68] Prémaud A, Le Meur Y, Debord J, Szelag J-C, Rousseau A, Hoizey G, et al. Maximum a posteriori Bayesian estimation of mycophenolic acid pharmacokinetics in renal transplant recipients at different postgrafting periods. Ther Drug Monit 2005;27(3):354–61.
[69] Mbo'o CP, Hameyer K. Fault diagnosis of bearing damage by means of the linear discriminant analysis of stator current features from the frequency selection. IEEE Trans Ind Appl 2016;52(5):3861–8.
[70] Ali L, Zhu C, Zhang Z, Liu Y. Automated detection of Parkinson's disease based on multiple types of sustained phonations using linear discriminant analysis and genetically optimized neural network. IEEE J Transl Eng Health Med 2019;7:1–10.
[71] ASCE. Seismic evaluation and retrofit of existing buildings (ASCE/SEI 41-17). American Society of Civil Engineers; 2017.
[72] Rasmussen CE. Gaussian processes in machine learning. In: Summer school on machine Learning. Springer; 2003, p. 63–71.
[73] Fan J, Upadhye S, Worster A. Understanding receiver operating characteristic (ROC) curves. Canad J Emerg Med 2006;8(1):19–20. http://dx.doi.org/10.1017/s1481803500013336.
[74] Mendler A, Döhler M, Ventura CE. A reliability-based approach to determine the minimum detectable damage for statistical damage detection. Mech Syst Signal Process 2021;154:107561.